nature physics

Article

https://doi.org/10.1038/s41567-024-02683-x

Highly anisotropic superconducting gap near the nematic quantum critical point of $FeSe_{1-x}S_x$

Received: 28 May 2024

Accepted: 27 September 2024

Published online: 13 November 2024

Check for updates

Pranab Kumar Nag[1,2,10], Kirsty Scott[1,2,10], Vanuildo S. de Carvalho[3], Journey K. Byland[4], Xinze Yang[1,2], Morgan Walker[1,2,4], Aaron G. Greenberg[1,2], Peter Klavins[4], Eduardo Miranda[5], Adrian Gozar[1,2,6], Valentin Taufour[4], Rafael M. Fernandes[7,9] & Eduardo H. da Silva Neto[1,2,4,8]

Nematic phases, in which electrons in a solid spontaneously break rotational symmetry while preserving translational symmetry, exist in several families of unconventional superconductors. Superconductivity mediated by nematic fluctuations is well established theoretically, but it has yet to be unambiguously identified experimentally. One major challenge is that nematicity is often intertwined with other degrees of freedom, such as magnetism and charge order. The $FeSe_{1-x}S_x$ family of superconductors provides an opportunity to explore this concept, as it features an isolated nematic phase that can be suppressed by sulfur substitution at a quantum critical point where the nematic fluctuations are the largest. Here we determine the momentum structure of the superconducting gap near the centre of the Brillouin zone in $FeSe_{0.81}S_{0.19}$—close to the quantum critical point—and find that it is anisotropic and nearly nodal. The gap minima occur in a direction that is rotated 45° with respect to the Fe–Fe direction, unlike the usual isotropic gaps due to spin-mediated pairing in other tetragonal Fe-based superconductors. Instead, we find that the gap structure agrees with theoretical predictions for superconductivity mediated by nematic fluctuations, indicating a change in the pairing mechanism across the phase diagram of $FeSe_{1-x}S_x$.

Showing some of the clearest realizations of nematicity among unconventional superconductors[1,2], Fe-based superconductors (FeSCs) are the most promising materials to search for superconductivity mediated by nematic fluctuations[3–9]. However, in most FeSCs the nematic phase appears in tandem with spin density wave (SDW) order, the fluctuations of which are often the dominant interaction mediating Cooper pairing[3]. For instance, in the archetypal $BaFe_2As_2$ system superconductivity is strongest when the concomitant magnetic and nematic phases are suppressed by doping or pressure[10,11]. Near such quantum critical points (QCPs), either spin or nematic fluctuations can theoretically promote superconductivity, yet spin fluctuations prevail, yielding nearly isotropic superconducting gaps in momentum space. Nevertheless, even when spin-mediated pairing is dominant, nematic fluctuations may still participate in the pairing mechanism—potentially even enhancing the superconducting transition temperature (T_c). Thus, elucidating the relationship between nematic fluctuations and superconductivity is crucial, especially for unconventional superconductors in which nematicity exists, including FeSCs, high-T_c cuprates and twisted bilayer graphene[12,13].

A full list of affiliations appears at the end of the paper. e-mail: eduardo.dasilvaneto@yale.edu

https://doi.org/10.1038/s41567-024-02683-x

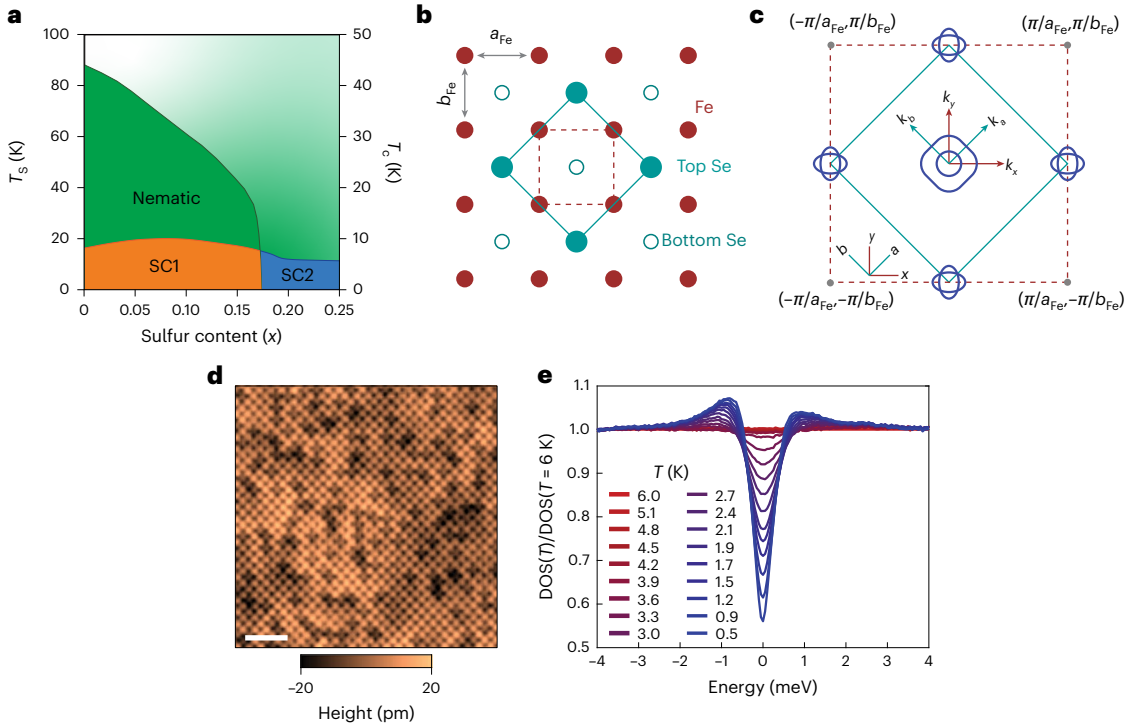

Fig. 1 | Phase diagram of $FeSe_{1-x}S_x$, and the crystal and electronic structure of superconducting $FeSe_{0.81}S_{0.19}$. a, Phase diagram of $FeSe_{1-x}S_x$ indicating the nematic/structural (tetragonal to orthorhombic) and superconducting transitions, T_S and T_c. For better visualization, we show T_S and T_c on separate scales. The green gradient schematically represents the intensity of nematic fluctuations. **b**, Schematic top view of the crystal structure of tetragonal $FeSe_{1-x}S_x$. S atoms are expected to be randomly positioned on Se locations but are omitted for clarity. Dashed lines represent the 1-Fe unit cell and solid lines show the actual crystallographic 2-Fe unit cell. **c**, Schematic of the Fermi surface of tetragonal $FeSe_{1-x}S_x$. The sizes of the pockets were enlarged by a factor of two in momentum space. **d**, Representative constant-current topographic image of $FeSe_{0.81}S_{0.19}$ showing the atomically resolved (Se,S) termination layer. The S atoms are seen as cross-like features in the data. Scale bar, 20 Å. **e**, Spatially averaged density of states (DOS) of $FeSe_{0.81}S_{0.19}$ (DOS(T)/DOS(T = 6 K)) showing the suppression of the superconducting gap with temperature. Panel **a** adapted from ref. 15 under a Creative Commons license CC BY 4.0.

The close coupling of SDW and nematic phases in most FeSCs hinders our ability to disentangle the relationship between nematic fluctuations and superconductivity, despite the strong evidence for nematic quantum criticality in compounds such as doped $BaFe_2As_2$ (ref. 14). However, the $FeSe_{1-x}A_x$ system (A = S or Te) presents a notable exception as its nematic phase is decoupled from magnetism[15–17]. In $FeSe_{1-x}S_x$, substituting S for Se suppresses the nematic phase towards a putative QCP at a sulfur concentration $x = x_c \approx 0.17$ (refs. 18–21; Fig. 1a), whereas the SDW phase is absent without the application of pressure[15,16,22]. Unlike the enhanced T_c at the putative SDW QCP in doped $BaFe_2As_2$, there is no obvious enhancement of superconductivity near x_c in $FeSe_{1-x}S_x$, which could at first suggest that nematic fluctuations do not mediate pairing. However, while pairing mediated by quantum critical fluctuations is expected to exhibit a T_c increase as the QCP is approached from the disordered side, T_c can rise or fall on entering the ordered state depending on whether the ordered state competes or cooperates with superconductivity[23]. It is worth noting that the cooperation scenario in $FeSe_{1-x}S_x$ has been observed in experiments that demonstrated an increase in the orthorhombic distortion below T_c for $x < x_c$ (ref. 24), which is consistent with the absence of a T_c maximum at x_c and in sharp contrast with the observed suppression of orthorhombic distortion below T_c in Co-doped $BaFe_2As_2$ (ref. 25). Interestingly, the maximum T_c in $FeSe_{1-x}S_x$ occurs deep inside the nematic state, near $x = 0.1$ (refs. 26,27), where spin fluctuations are also strongest[28]. The momentum space (**k**) structure of the gap in FeSe, obtained by scanning tunnelling microscopy and spectroscopy (STM and STS) measurements, is also consistent with superconductivity mediated by spin fluctuations[29–31]. However, changes in the superconducting gap and electronic structure (supported by tunnelling and thermodynamic measurements[32–34]) across x_c suggest different pairing mechanisms for superconductivity inside (SC1) and superconductivity outside (SC2) the long-range nematic state. Thus, while there is abundant evidence for spin-mediated pairing in SC1, the pairing interaction near the nematic QCP, and in SC2 generally, remains unknown.

Despite potentially holding the key to unravelling the existence of superconductivity mediated by nematic fluctuations, the gap function $\Delta(\mathbf{k})$ for $x \gtrsim x_c$, where nematic fluctuations peak[16], remains to be determined. One of the difficulties is that the average gap in the SC2 region ($\Delta_{avr} \approx \pm 0.8$ meV) is much smaller than in FeSe ($\Delta_{avr} \approx \pm 2.5$ meV) and typical pnictide FeSCs ($\Delta_{avr} \approx \pm 4$–$12$ meV), which has precluded the spectroscopic determination of $\Delta(\mathbf{k})$ in SC2 in previous studies[32]. Here we use sub-kelvin STM and STS to measure the momentum structure of the superconducting gap in $FeSe_{0.81}S_{0.19}$ with high energy resolution. Our main finding is that the gap structure for $FeSe_{1-x}S_x$ near the nematic QCP is highly anisotropic with deep minima along a direction 45° from the Fe–Fe directions. This is in contrast to other tetragonal FeSCs in the vicinity of a QCP, in which the gaps on the hole pockets are nearly isotropic or show shallow minima along the Fe–Fe direction, or both[35,36]. The observed gap structure in general contradicts theoretical predictions based on the spin-fluctuation scenario[37–44], yet aligns with predictions for superconductivity mediated by nematic fluctuations[5,8].

The crystal structure of $FeSe_{1-x}S_x$ is orthorhombic inside the nematic phase and tetragonal outside. Both 1-Fe (dashed squares) and 2-Fe (solid squares) unit cells (Fig. 1b) and corresponding Brillouin zones (Fig. 1c) are used in the literature. In the nematic phase, the two orthogonal Fe–Fe bonds become non-equivalent, $a_{Fe} \neq b_{Fe}$. We denote the Fe–Fe directions as x and y, and the 2-Fe unit cell axes as a and b (Fig. 1c). The Fermi surface of tetragonal $FeSe_{1-x}S_x$ features two hole-like bands surrounding the Γ point and two electron-like bands at the M points of the 2-Fe unit cell[15]. To investigate the influence of nematic fluctuations on the superconductivity in SC2, we focused on $FeSe_{0.81}S_{0.19}$ near the

https://doi.org/10.1038/s41567-024-02683-x

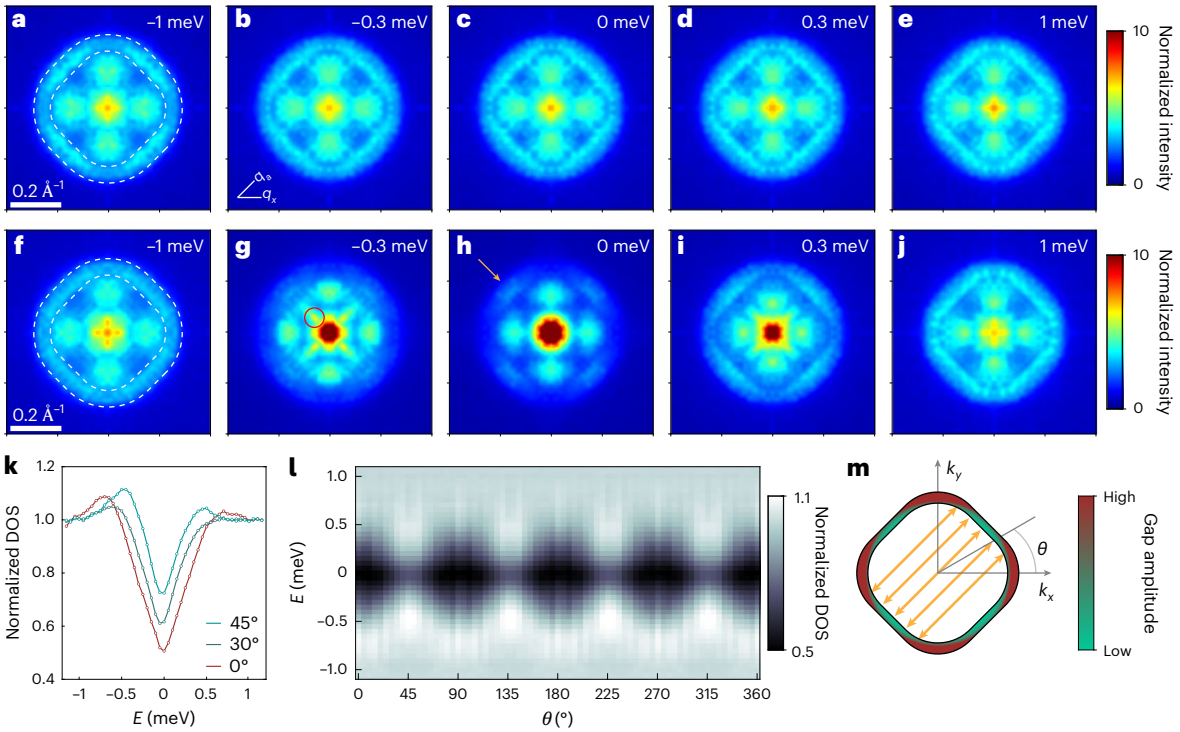

Fig. 2 | QPI from the superconducting state in $FeSe_{0.81}S_{0.19}$ and identification of the gap anisotropy. a–**e**, $g(\mathbf{q},E)$ measured in the non-superconducting state at $B = 3$ T at $E = -1$ meV (**a**), 0.3 meV (**b**), 0 meV (**c**), 0.3 meV (**d**) and 1 meV (**e**). **f**–**j**, Corresponding $g(\mathbf{q},E)$ measured in the superconducting state $B = 0$ T. **k**, DOS from the rounded-square QPI pattern (for example, the area between the dashed lines in **f**) along different θ, revealing an anisotropic gap structure. **l**, DOS map as a function of E and θ from the rounded-square pattern, clearly showing gap minima along 45°, 135°, 225° and 315°. **m**, Schematic of an anisotropic gap on a rounded-square Fermi surface. The gap minima occur at the directions indicated in **l**. Orange arrows indicate various scattering processes contributing to the intensity of the square pattern along $\theta = 0°$.

putative nematic QCP. A representative topographic STM image of the Se termination is shown in Fig. 1d, in which S atoms appear as densely distributed cross-like features at Se sites. Temperature-dependent spectroscopy revealed the suppression of the spatially averaged superconducting gap with increasing temperature (Fig. 1e).

Direction of the superconducting gap minima

To probe the momentum structure of the superconducting gap, we used STS to measure quasiparticle interference (QPI) patterns in $FeSe_{0.81}S_{0.19}$. QPI appears as periodic modulations of the DOS[45], with energy (E)-dependent wave vectors, $\mathbf{q}(E)$ reflecting constant-energy scattering processes between different initial ($\mathbf{k}_i$) and final ($\mathbf{k}_f$) momentum states. The Fourier transform of the STS images, $g(\mathbf{q},E)$, reveals patterns that have been widely used to image band structures, nematicity and stripe-like states in $FeSe_{1-x}S_x$ (refs. 29,32,46–48). Figure 2a–e shows $g(\mathbf{q},E)$ at a magnetic field $B = 3$ T (non-superconducting state). At $E = -1.0$ meV, a rounded-square pattern appears (see the area between the two dashed white lines in Fig. 2a) and shrinks towards $E = 1$ meV (Fig. 2e). Its shape and hole-like dispersion are consistent with intra-band scattering originating from the outer pocket at $k_z = 0$ (Γ point), as described in Supplementary Note I). In the superconducting state ($B = 0$ T), $g(\mathbf{q},E)$ patterns (Fig. 2f–j) change substantially for energies inside the gap. We divide our discussion into two regions: region I (rounded-square contour) and region II (smaller momenta inside the inner white dashed square in Fig. 2a). In region II, which we discuss in detail later, superconductivity induces new peaks, such as the one marked by the red circle in Fig. 2g from Bogoliubov QPI (BQPI). In region I, the relative intensity between points along the a and x directions changes from nearly equal at $E = \pm 1$ meV (Fig. 2f,j) to the intensity along a dominating over the intensity along x near $E = 0$ meV (Fig. 2g–i), as indicated by the orange arrow in Fig. 2h. This observation prompted us to analyse the energy-dependent DOS of the rounded-square QPI feature for different azimuthal angles θ, defined as the angle from k_x towards k_a. Under this definition, the gap on the Γ pocket of FeSe, which is two-fold symmetric, has minima along $\theta = 90°$ and 270° (that is, along y or x depending on the nematic domain)[29,49]. In contrast, for $FeSe_{0.81}S_{0.19}$, our analysis revealed a smaller gap at $\theta = 45°$ than at $\theta = 0°$ (that is, along the a and b axes) (Fig. 2k,l). At first, one might be tempted to interpret the finite size of the QPI-extracted gap at 45° as evidence for the absence of a node. However, the spectral intensity at 45° on the square contour of $g(\mathbf{q},E)$ involves contributions from various $\mathbf{k}$ points on the Fermi surface, which have varying gap sizes (as depicted schematically in Fig. 2m). Therefore, the location of the coherence peaks for the 45° gap (approximately ±450 μeV) represents an upper bound on the gap magnitude along a or b, leaving the possibility of a nodal structure open. Regardless, this θ dependence indicates a fundamental change in gap structure from SC1 to the nematic QCP in SC2.

The gap minima directions in $FeSe_{0.81}S_{0.19}$ can also be identified by analysing the BQPI signal in region II. When a superconducting gap is anisotropic in $\mathbf{k}$ space, the Bogoliubov quasiparticle momentum structure exhibits closed constant-energy contours that are distinct from their normal state counterparts. For a given E, each contour has two points of maximum DOS that are anchored to the underlying Fermi surface where $|\Delta(\mathbf{k})| = |E|$. For the rounded-square Fermi surface obtained from the $g(\mathbf{q},E)$ maps, the closed-energy contours promote seven BQPI wave vectors $\mathbf{q}_i$ that connect eight points of high DOS, similar to the celebrated octet model for cuprates[45,50,51]. Among these vectors, $\mathbf{q}_7$ (blue arrow in Fig. 3a) is particularly important for identifying gap minima directions. For instance, in the case of a nodal gap, $\mathbf{q}_7$ indicates the gap minima direction and is the only wave vector that decreases to zero length at $E = 0$. To identify the direction of $\mathbf{q}_7$, we compared $g(\mathbf{q},E)$ along the two high-symmetry directions, a and x (Fig. 3b,c), with their

https://doi.org/10.1038/s41567-024-02683-x

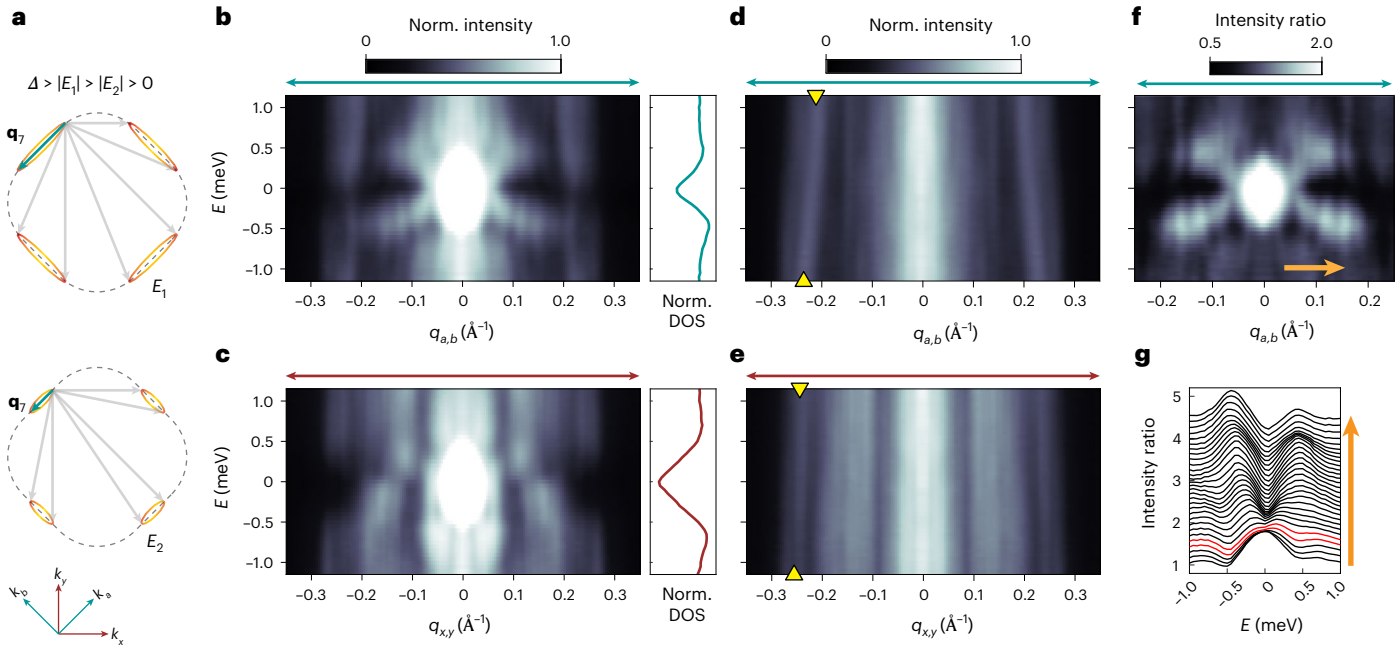

Fig. 3 | Bogoliubov QPI in $FeSe_{0.81}S_{0.19}$. **a**, Schematic representation of constant-energy contours in the superconducting state at two different energies (E_1 and E_2). The red colour at the tips of the contours represents the larger DOS at those points. **b**–**e**, Dispersion plots measured at $B = 0$ T (**b**,**c**) and $B = 3$ T (**d**,**e**) along the *a*,*b* direction (**b**,**d**) and the *x*,*y* direction (**c**,**e**) as defined in Fig. 1. The insets on the right in **b** and **c** are the gaps on the square contours of $g(\mathbf{q},E)$, also shown in Fig. 2k. The yellow triangles delimit the dispersion of the rounded-square feature shown in Fig. 2a–e. Norm., normalized. **f**, Dispersion plot of $\mathbf{q}_7$ obtained by dividing the $B = 0$ T data (**b**) by the $B = 3$ T data (**d**). The horizontal double arrows in **b**-**f** denote the directions for which the dispersions are plotted, along a,b (blue) and along x,y (red), as defined by the axes in **a**. **g**, Constant **q** cuts of the data in **f**, shifted vertically for clarity. The range of momenta shown in **g** is from 0.0384 Å^{-1} to 0.1557 Å^{-1} (marked by the orange arrow in **f**) at equally spaced steps of 0.0040 Å^{-1}. The red curves in **g** show the lowest momenta (0.0505 Å^{-1} and 0.0546 Å^{-1}) where a two-peak structure is clearly observed.

non-superconducting counterparts (Fig. 3d,e). These dispersion plots show various superconductivity-induced modifications to $g(\mathbf{q},E)$ within gap energies. The outermost QPI feature (largest $|\mathbf{q}|$, yellow triangles in Fig. 3d,e) in the non-superconducting state corresponds to the rounded-square Fermi surface, whereas peaks at smaller $|\mathbf{q}|$ probably originate from other bands (Fig. 3d,e). The most salient feature of these plots is the emergence of a BQPI feature along $q_{a,b}$ that decreases towards $|\mathbf{q}| = 0$ at $E = 0$ and is approximately symmetric across the Fermi level (Fig. 3b). In contrast, no such feature exists along the $q_{x,y}$ direction (Fig. 3c). This X pattern, confirmed by multiple measurements and under various experimental conditions (Supplementary Note II), clearly identifies *a* and *b* (that is $\theta = 45°$) as the smallest gap directions, consistent with the analysis in Fig. 2.

Superconducting gap structure from BQPI

After identifying the gap minima direction in $FeSe_{0.81}S_{0.19}$, we used the measured $\mathbf{q}_7$ dispersion to construct the angular dependence of the gap magnitude, $|\Delta(\theta)|$. Spatial inhomogeneity and other band features can blur $\mathbf{q}_7$ at small $\mathbf{q}$. To mitigate this, we divided the $B = 0$ T dispersion map (Fig. 3b) by the $B = 3$ T map (Fig. 3d) to create a normalized dispersion map (Fig. 3f). The resulting $\mathbf{q}_7(E)$ dispersion was then geometrically inverted to determine $|\Delta(\theta)|$, an established technique to determine gap structures in other unconventional superconductors[29,51,52]. As detailed in Supplementary Note III, we analysed individual constant $\mathbf{q}$ cuts (Fig. 3g), in which each $\mathbf{q}_7$ value mapped to a θ value with a corresponding gap amplitude that was determined by the peak locations in Fig. 3g. This analysis extracted $|\Delta(\theta)|$ for the outer Γ pocket from the BQPI data over a wide range of θ, as shown in Fig. 4a.

Superconducting gap from nematic fluctuations

To deduce the pairing interaction in $FeSe_{0.81}S_{0.19}$, we compared experimentally obtained $|\Delta(\theta)|$ with the angular dependence of the gap expected for the two leading pairing candidates: nematic and spin fluctuations. First we considered the nematic-fluctuation scenario, motivated by the fact that the nematic transition temperature is suppressed to zero at $x = x_c \approx 0.17$, which coincides with a regime of strongly enhanced nematic fluctuations[16]. The distinguishing feature of electronic interactions mediated by nematic fluctuations is the nematic form factor $f(\theta) = \lambda\cos(2\theta)$, which describes the coupling between electronic and nematic degrees of freedom. Enforced by the tetragonal symmetry of the lattice, this form factor leads to so-called cold spots at $\theta = 45°$ (and symmetry-related points) on any Fermi pocket centred at the Γ point. At these cold spots, electrons are nearly decoupled from critical nematic fluctuations, as $f(45°) = 0$. Consequently, if pairing is mediated by nematic fluctuations, the gap should be substantially suppressed at these cold spots, as discussed in refs. 5,8. Motivated by these results, we considered the following phenomenological form for the gap function at the central hole pocket:

$$\Delta(\theta) = \Delta_s + \Delta_s'\cos^2(2\theta), \quad (1)$$

where Δ_s and Δ_s' represent the amplitudes of the isotropic and anisotropic components to the gap function, repectively. To test this idea, we fitted equation (1) to the experimental data, as shown in Fig. 4a,b. We found that equation (1) not only accurately described the data, but also yielded a large ratio of $\Delta_s'/\Delta_s \approx 8$. This large ratio implies a strong decrease in the gap at the cold spots, and is thus consistent with pairing dominated by nematic fluctuations.

To go beyond this qualitative description, we followed ref. 8 and employed an Eliashberg approach to solve a simple model in which pairing on the hole pocket is mediated by quantum critical nematic fluctuations (see Supplementary Note V for details), without presuming a specific form of $\Delta(\theta)$. While the nematic form factor vanished at cold spots ($\theta = 45°$), the temporal fluctuations of the nematic order

https://doi.org/10.1038/s41567-024-02683-x

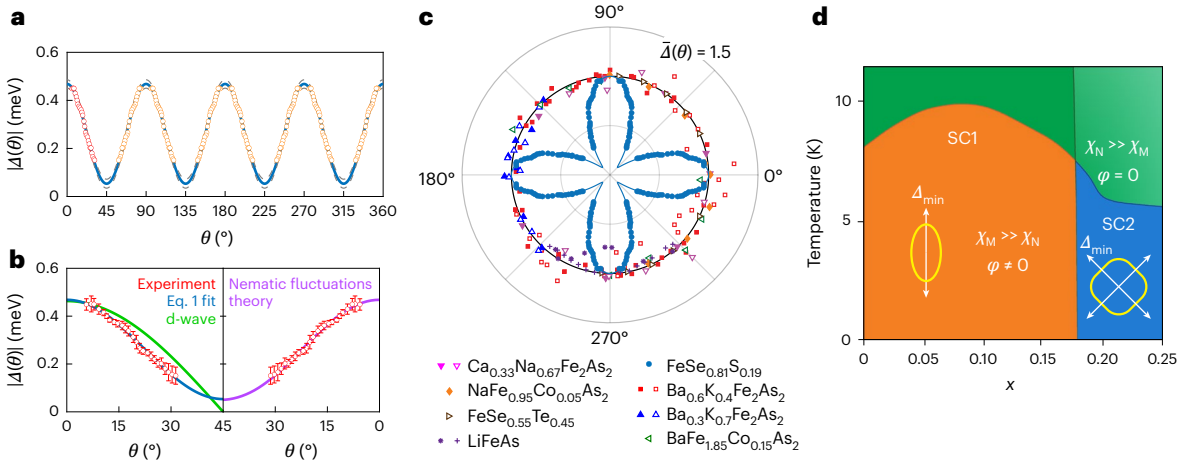

Fig. 4 | Angular dependence of the superconducting gap in $FeSe_{0.81}S_{0.19}$. **a**, $|\Delta(\theta)|$ obtained from BQPI data (see Supplementary Note V for details). The red data points between 0° and 45° are repeated for all other equivalent angles (orange data points). The blue line is a least-squares fit of equation (1) to the data, yielding $\Delta_s' = 0.42 \pm 0.02$ meV and $\Delta_s = 0.05 \pm 0.01$ meV, and the uncertainties were obtained from the 95% confidence intervals of the fit. The grey dashed lines represent the 95% confidence range for the fit. **b**, $|\Delta(\theta)|$ data in **a** with error bars that represent 95% confidence intervals obtained from fitting Gaussian functions plus a linear background to the data in **b**. The fits from equation (1) (blue, same as in **d**) and the *d*-wave function $\Delta(\theta) = \Delta_d \cos(2\theta)$ (green, fitted to the three lowest θ values; see Supplementary Note VI) are shown (left) as well as the theoretical calculation that considers pairing due to nematic quantum critical fluctuations (right) (purple, see Supplementary Note V). **c**, Polar plots comparing the normalized gap $|\bar{\Delta}(\theta)|$ in $FeSe_{0.81}S_{0.19}$ (outer hole pocket, full circles) and in various tetragonal FeSCs (data from refs. 35,36). The gaps for the largest (stars[35]) and middle (crosses[36]) pockets at Γ in LiFeAs (which has three pockets) are depicted, with the reported anisotropic gaps normalized to their respective maxima. For the other materials, open (filled) symbols represent $|\bar{\Delta}(\theta)|$ for outer (inner) hole pockets. See Extended Data Fig. 1 for the data plotted without normalization. **d**, Phase diagram of $FeSe_{1-x}S_x$ with the white arrows depicting the direction of Δ_{min} on the hole Fermi surfaces in SC1 and SC2, and the presence or absence of magnetic fluctuations (χ_M), nematic order (φ) and nematic fluctuations (χ_N), as discussed in the text.

parameter endowed them with a finite gap value, consistent with ref. 8. Although this low-energy model did not capture the complexity of the band structure of the FeSCs, it has the advantage of having only two parameters: the distance to the putative QCP, r_0, and the dimensionless nematic coupling constant, λ. The generic behaviour of the gap function that solves the Eliashberg equations shows deep minima along 45°, demonstrating that this is a robust feature of the nematic-fluctuation scenario. The gap anisotropy is robust for r_0 around $r_0 = 0$ (Supplementary Note V), implying that small deviations from the nematic QCP should not drastically change the gap form. The value of λ controls the depth of the gap minima, and, as a result, the functional form of the gap. As shown in Fig. 4b (right-hand side), for a moderate $\lambda = 0.1$, the calculated gap function agreed well with the data and approximated the form proposed in equation (1).

Spin-fluctuation scenarios

Given their primary role in other FeSCs, it is important to discuss the role of spin fluctuations in the $FeSe_{1-x}S_x$ phase diagram and whether they can produce a gap like that described in equation (1). Although nematic fluctuations diverge at x_c (ref. 16), NMR experiments show that spin fluctuations are suppressed above $x = 0.09$ (ref. 28), indicating a substantial increase in the relative strength of nematic fluctuations over spin fluctuations at the QCP for $FeSe_{0.81}S_{0.19}$. Recent transport measurements further corroborated the absence of magnetic quantum critical fluctuations in unpressurized $FeSe_{1-x}S_x$ (ref. 17). Parallel to this experimental context, we also found that the gap functions from spin fluctuations, as predicted by theory, disagreed with the data. To see this, we noted that spin fluctuations in FeSCs are expected to promote a sign-changing gap[3], which can be either a *d* wave or $s^{\pm}$ gap[53,54]. The former emerges when the low-energy spin fluctuations peak at (π,π) in the 1-Fe Brillouin zone, whereas the latter appears when the peak is at $(\pi,0)/(0,\pi)$. Neutron scattering on undoped FeSe shows that $(\pi,0)/(0,\pi)$ fluctuations dominate at low energies, and (π,π) fluctuations only become relevant at high energies[55–57], which poses challenges to a *d*-wave scenario. Moreover, a simple *d*-wave function, $\Delta(\theta) = \Delta_d \cos(2\theta)$, did not fit the data (green line in Fig. 4b and Supplementary Note VI), although including higher harmonics could slightly alter this basic functional form.

As for the $s^{\pm}$ gap structure generated by $(\pi,0)/(0,\pi)$ spin fluctuations, predictions based on various theoretical approaches and for diverse parameter ranges invariably result in hole pockets with nearly isotropic gaps or gaps with minima along the Fe–Fe direction[37–44]. Such a weakly anisotropic gap was also consistently observed in tetragonal FeSCs near a putative SDW quantum phase transition, as shown in Fig. 4c. Although, in principle, a highly anisotropic gap like the one we observed might be possible in an $s^{\pm}$ scenario, it would require extreme parameter fine-tuning, as shown by the fact that such a gap has not been realized in currently available model calculations. In contrast, the gap structure observed in $FeSe_{0.81}S_{0.19}$ is naturally satisfied in the case of pairing mediated by nematic fluctuations for very general parameter ranges, as discussed earlier. We emphasize that prominent pairing from nematic fluctuations does not imply that spin fluctuations are irrelevant. In fact, because nematic fluctuations peak at zero momentum, whereas spin fluctuations peak at large momentum, the latter are probably relevant to determine the relative sign between the gaps on the hole and electron pockets.

Conclusions

Superconductivity mediated by nematic fluctuations offers the most natural explanation for the gap structure revealed by our STS measurements. The near-nodal gap with minima along 45° appears near a nematic QCP and away from region of maximum spin fluctuations, in qualitative contrast to the gaps in other tetragonal FeSCs in which nematic and SDW phases are tightly coupled (Fig. 4c and Extended Data Fig. 1). Furthermore, while spin-mediated $s^{\pm}$ models predict isotropic gaps or minima along the Fe–Fe direction, the gap structure in $FeSe_{0.81}S_{0.19}$ aligns precisely with the nematic-fluctuation theory (Fig. 4a–c).

Our results are also consistent with recent calculations that showed that the superconducting state mediated by quantum critical

nematic fluctuations displays enhanced quasiparticle excitations at very low energies due to the nematic cold spots located at $\theta = 45°$ (ref. 58). This enhanced low-energy DOS leads to a specific heat with a temperature dependence that matches thermodynamic data for $FeSe_{1-x}S_x$ near x_c (ref. 59). On the other hand, the enhanced DOS near $E = 0$ meV (see Fig. 1e and refs. 32,59) has also been proposed to emerge from an ultranodal superconducting state with Bogoliubov Fermi surfaces[60–62]. Although our data cannot confirm or rule out the ultranodal scenario, our measurements indicate that low-temperature spectroscopic measurements with an energy resolution better than approximately 150 μeV may be required to address this question (Supplementary Note VII).

We also propose a holistic phenomenological description of $FeSe_{1-x}S_x$, consistent with various theoretical and experimental studies of superconductivity, nematicity and spin fluctuations, as summarized in Fig. 4d. For small x (SC1 region), $(\pi,0)/(0,\pi)$ spin fluctuations (described by χ_M) dominate pairing, as indicated by neutron scattering measurements of the spin resonance across T_c (refs. 55–57) and by NMR studies that correlate the maximum T_c to peak spin fluctuations near $x = 0.09$ (ref. 28). The strong two-fold anisotropy of the gap in FeSe, with sharp minima along the x or y directions observed by STS[29] and angle-resolved photoemission spectroscopy[49], can be explained by the combined effects of long-range nematicity (order parameter φ) and spin fluctuations[30] on the pairing state. Thus, for $x < x_c$, it is the combination of φ and χ_M that gives rise to a gap with strong minima along the x or y directions in the SC1 state. On the other hand, across x_c, there is no nematic order ($\varphi = 0$) and χ_M is relatively suppressed[28]. Conversely, it is χ_N that become large in the vicinity of the QCP, as determined by elastoresistance measurements[16]. Under these conditions, nematic fluctuations become important for the pairing interaction, and the gap structure at the QCP just outside SC1 becomes strongly anisotropic, with gap minima along a and b, as our experiments show. Therefore, it is likely that nematicity plays an important dual role in superconductivity in $FeSe_{1-x}S_x$, with long-range nematic order inducing gap minima along x or y but nematic fluctuations inducing near-nodes along a and b.

In this work we resolved the angular dependence of the superconducting gap on the outer Γ hole pocket, the magnitude of which is much smaller than in other FeSCs (Extended Data Fig. 1). Our BQPI measurements indicate even smaller gaps on the inner Γ hole pocket and the M point electron pockets, but we cannot resolve their momentum structures (Supplementary Note VII). However, the gap structure on the electron pockets is not ideal for determining the influence of nematic fluctuations on pairing as hybridization effects and the considerable d_{xy} spectral weight at the M point can cause the gap minima to happen either along x,y or a,b, regardless of nematic cold spots (see Supplementary Note VIII and ref. 9). Similarly, in KFe_2As_2, which is far from either a nematic or a SDW QCP and displays only hole pockets, a combination of spin–orbit coupling and a large Hund's coupling[63] has been proposed as the cause of the accidental nodes away from the Fe–Fe direction[64,65]. In contrast, in $FeSe_{0.81}S_{0.19}$ and most other tetragonal FeSCs near magnetic or nematic QCPs displaying hole and electron pockets, the quasi-circular hole pockets at Γ, (composed solely of d_{xz} and d_{yz} orbitals) are not affected by these issues, allowing the gap structure on these pockets to more directly reveal the influence of nematic fluctuations on pairing. Thus we also expect the gap structure on the inner hole pocket to be similar to that on the outer hole pocket. Future measurements that resolve the momentum structure of the superconducting gap on all Fermi surface pockets would enable direct comparisons to theoretical models that fully capture the complexity of FeSC band structures and the combined effects of nematic and spin fluctuations, allowing further verification of the nematic-fluctuation pairing scenario suggested by our findings. Systematic studies of gap structures across SC2 could also test how this scenario evolves with increasing x and determine whether the gap structure observed near the QCP is ubiquitous to SC2, as is suggested by the absence of abrupt changes in superconducting properties for $x > x_c$. Overall, our work introduces an approach that can be extended to test this and other scenarios in $FeSe_{1-x}S_x$ and to study the relationship between nematic fluctuations and superconductivity in other quantum materials.

Online content

Any methods, additional references, Nature Portfolio reporting summaries, source data, extended data, supplementary information, acknowledgements, peer review information; details of author contributions and competing interests; and statements of data and code availability are available at https://doi.org/10.1038/s41567-024-02683-x.

References

1. Fradkin, E., Kivelson, S. A., Lawler, M. J., Eisenstein, J. P. & Mackenzie, A. P. Nematic Fermi fluids in condensed matter physics. *Annu. Rev. Condens. Matter Phys.* **1**, 153–178 (2010).
2. Fernandes, R., Chubukov, A. & Schmalian, J. What drives nematic order in iron-based superconductors? *Nat. Phys.* **10**, 97–104 (2014).
3. Fernandes, R. M. et al. Iron pnictides and chalcogenides: a new paradigm for superconductivity. *Nature* **601**, 35–44 (2022).
4. Böhmer, A. E., Chu, J.-H., Lederer, S. & Yi, M. Nematicity and nematic fluctuations in iron-based superconductors. *Nat. Phys.* **18**, 1412–1419 (2022).
5. Lederer, S., Schattner, Y., Berg, E. & Kivelson, S. A. Enhancement of superconductivity near a nematic quantum critical point. *Phys. Rev. Lett.* **114**, 097001 (2015).
6. Metlitski, M. A., Mross, D. F., Sachdev, S. & Senthil, T. Cooper pairing in non-Fermi liquids. *Phys. Rev. B* **91**, 115111 (2015).
7. Lederer, S., Schattner, Y., Berg, E. & Kivelson, S. A. Superconductivity and non-Fermi liquid behavior near a nematic quantum critical point. *Proc. Natl Acad. Sci. USA* **114**, 4905–4910 (2017).
8. Klein, A. & Chubukov, A. Superconductivity near a nematic quantum critical point: interplay between hot and lukewarm regions. *Phys. Rev. B* **98**, 220501 (2018).
9. Kang, J. & Fernandes, R. M. Superconductivity in FeSe thin films driven by the interplay between nematic fluctuations and spin-orbit coupling. *Phys. Rev. Lett.* **117**, 217003 (2016).
10. Shibauchi, T., Carrington, A. & Matsuda, Y. A quantum critical point lying beneath the superconducting dome in iron pnictides. *Annu. Rev. Condens. Matter Phys.* **5**, 113–135 (2014).
11. Hayes, I. M. et al. Scaling between magnetic field and temperature in the high-temperature superconductor $BaFe_2(As_{1-x}P_x)_2$. *Nat. Phys.* **12**, 916–919 (2016).
12. Keimer, B., Kivelson, S. A., Norman, M. R., Uchida, S. & Zaanen, J. From quantum matter to high-temperature superconductivity in copper oxides. *Nature* **518**, 179–186 (2015).
13. Andrei, E. Y. & MacDonald, A. H. Graphene bilayers with a twist. *Nat. Mater.* **19**, 1265–1275 (2020).
14. Worasaran, T. et al. Nematic quantum criticality in an Fe-based superconductor revealed by strain-tuning. *Science* **372**, 973–977 (2021).
15. Coldea, A. I. Electronic nematic states tuned by isoelectronic substitution in bulk $FeSe_{1-x}S_x$. *Front. Phys.* **8**, 528 (2021).
16. Hosoi, S. et al. Nematic quantum critical point without magnetism in $FeSe_{1-x}S_x$ superconductors. *Proc. Natl Acad. Sci. USA* **113**, 8139–8143 (2016).
17. Ayres, J. et al. Transport evidence for decoupled nematic and magnetic criticality in iron chalcogenides. *Commun. Phys.* **5**, 100 (2022).
18. Licciardello, S. et al. Electrical resistivity across a nematic quantum critical point. *Nature* **567**, 213–217 (2019).
19. Huang, W. K. et al. Non-Fermi liquid transport in the vicinity of the nematic quantum critical point of superconducting $FeSe_{1-x}S_x$. *Phys. Rev. Res.* **2**, 033367 (2020).

20. Zhang, W. et al. Quadrupolar charge dynamics in the nonmagnetic $FeSe_{1-x}S_x$ superconductors. *Proc. Natl Acad. Sci. USA* **118**, e2020585118 (2021).
21. Chibani, S. et al. Lattice-shifted nematic quantum critical point in $FeSe_{1-x}S_x$. *npj Quantum Mater.* **6**, 37 (2021).
22. Matsuura, K. et al. Maximizing T_c by tuning nematicity and magnetism in $FeSe_{1-x}S_x$ superconductors. *Nat. Commun.* **8**, 1143 (2017).
23. Chen, X., Maiti, S., Fernandes, R. M. & Hirschfeld, P. J. Nematicity and superconductivity: competition versus cooperation. *Phys. Rev. B* **102**, 184512 (2020).
24. Wang, L. et al. Superconductivity-enhanced nematicity and "s+d" gap symmetry in $Fe(Se_{1-x}S_x)$. *Phys. Stat. Solidi B* **254**, 1600153 (2017).
25. Nandi, S. et al. Anomalous suppression of the orthorhombic lattice distortion in superconducting $Ba(Fe_{1-x}Co_x)_2As_2$ single crystals. *Phys. Rev. Lett.* **104**, 057006 (2010).
26. Ishida, K. et al. Pure nematic quantum critical point accompanied by a superconducting dome. *Proc. Natl Acad. Sci. USA* **119**, e2110501119 (2022).
27. Mukasa, K. et al. Enhanced superconducting pairing strength near a pure nematic quantum critical point. *Phys. Rev. X* **13**, 011032 (2023).
28. Wiecki, P. et al. Persistent correlation between superconductivity and antiferromagnetic fluctuations near a nematic quantum critical point in $FeSe_{1-x}S_x$. *Phys. Rev. B* **98**, 020507 (2018).
29. Sprau, P. O. et al. Discovery of orbital-selective Cooper pairing in FeSe. *Science* **357**, 75–80 (2017).
30. Kang, J., Fernandes, R. M. & Chubukov, A. Superconductivity in FeSe: the role of nematic order. *Phys. Rev. Lett.* **120**, 267001 (2018).
31. Benfatto, L., Valenzuela, B. & Fanfarillo, L. Nematic pairing from orbital-selective spin fluctuations in FeSe. *npj Quantum Mater.* **3**, 56 (2018).
32. Hanaguri, T. et al. Two distinct superconducting pairing states divided by the nematic end point in $FeSe_{1-x}S_x$. *Sci. Adv.* **4**, eaar6419 (2018).
33. Sato, Y. et al. Abrupt change of the superconducting gap structure at the nematic critical point in $FeSe_{1-x}S_x$. *Proc. Natl Acad. Sci. USA* **115**, 1227–1231 (2018).
34. Coldea, A. I. et al. Evolution of the low-temperature Fermi surface of superconducting $FeSe_{1-x}S_x$ across a nematic phase transition. *npj Quantum Mater.* **4**, 2 (2019).
35. Richard, P., Qian, T. & Ding, H. ARPES measurements of the superconducting gap of Fe-based superconductors and their implications to the pairing mechanism. *J. Phys. Condens. Matter* **27**, 293203 (2015).
36. Allan, M. P. et al. Anisotropic energy gaps of iron-based superconductivity from intraband quasiparticle interference in LiFeAs. *Science* **336**, 563–567 (2012).
37. Graser, S., Maier, T. A., Hirschfeld, P. J. & Scalapino, D. J. Near-degeneracy of several pairing channels in multiorbital models for the Fe pnictides. *N. J. Phys.* **11**, 025016 (2009).
38. Kuroki, K., Usui, H., Onari, S., Arita, R. & Aoki, H. Pnictogen height as a possible switch between high-T_c nodeless and low-T_c nodal pairings in the iron-based superconductors. *Phys. Rev. B* **79**, 224511 (2009).
39. Maier, T. A., Graser, S., Scalapino, D. J. & Hirschfeld, P. J. Origin of gap anisotropy in spin fluctuation models of the iron pnictides. *Phys. Rev. B* **79**, 224510 (2009).
40. Ikeda, H., Arita, R. & Kuneš, J. Phase diagram and gap anisotropy in iron-pnictide superconductors. *Phys. Rev. B* **81**, 054502 (2010).
41. Maiti, S., Korshunov, M. M., Maier, T. A., Hirschfeld, P. J. & Chubukov, A. V. Evolution of symmetry and structure of the gap in iron-based superconductors with doping and interactions. *Phys. Rev. B* **84**, 224505 (2011).
42. Yin, Z. P., Haule, K. & Kotliar, G. Spin dynamics and orbital-antiphase pairing symmetry in iron-based superconductors. *Nat. Phys.* **10**, 845–850 (2014).
43. Rhodes, L. C., Böker, J., Müller, M. A., Eschrig, M. & Eremin, I. M. Non-local d_{xy} nematicity and the missing electron pocket in FeSe. *npj Quantum Mater.* **6**, 45 (2021).
44. Fernández-Martín, R., Calderón, M. J., Fanfarillo, L. & Valenzuela, B. The role of orbital nesting in the superconductivity of iron-based superconductors. *Condens. Matter* **6**, 34 (2021).
45. Hoffman, J. et al. Imaging quasiparticle interference in $Bi_2Sr_2CaCu_2O_{8+\delta}$. *Science* **297**, 1148–1151 (2002).
46. Watashige, T. et al. Evidence for time-reversal symmetry breaking of the superconducting state near twin-boundary interfaces in FeSe revealed by scanning tunneling spectroscopy. *Phys. Rev. X* **5**, 031022 (2015).
47. Moore, S. A. et al. Evolution of the superconducting properties in $FeSe_{1-x}S_x$. *Phys. Rev. B* **92**, 235113 (2015).
48. Walker, M. et al. Electronic stripe patterns near the Fermi level of tetragonal Fe(Se,S). *npj Quantum Mater.* **8**, 60 (2023).
49. Liu, D. et al. Orbital origin of extremely anisotropic superconducting gap in nematic phase of FeSe superconductor. *Phys. Rev. X* **8**, 031033 (2018).
50. Wang, Q.-H. & Lee, D.-H. Quasiparticle scattering interference in high-temperature superconductors. *Phys. Rev. B* **67**, 020511 (2003).
51. McElroy, K. et al. Relating atomic-scale electronic phenomena to wave-like quasiparticle states in superconducting $Bi_2Sr_2CaCu_2O_{8+\delta}$. *Nature* **422**, 592–596 (2003).
52. Allan, M. et al. Imaging Cooper pairing of heavy fermions in $CeCoIn_5$. *Nat. Phys.* **9**, 468–473 (2013).
53. Hirschfeld, P. J., Korshunov, M. M. & Mazin, I. I. Gap symmetry and structure of Fe-based superconductors. *Rep. Progr. Phys.* **74**, 124508 (2011).
54. Chubukov, A. Pairing mechanism in Fe-based superconductors. *Annu. Rev. Condens. Matter Phys.* **3**, 57–92 (2012).
55. Wang, Q. et al. Magnetic ground state of FeSe. *Nat. Commun.* **7**, 12182 (2016).
56. Wang, Q. et al. Strong interplay between stripe spin fluctuations, nematicity and superconductivity in FeSe. *Nat. Mater.* **15**, 159–163 (2016).
57. Chen, T. et al. Anisotropic spin fluctuations in detwinned FeSe. *Nat. Mater.* **18**, 709–716 (2019).
58. Islam, K. R. & Chubukov, A. Unconventional superconductivity near a nematic instability in a multi-orbital system. *npj Quantum Mater.* **9**, 28 (2024).
59. Mizukami, Y. et al. Unusual crossover from Bardeen-Cooper-Schrieffer to Bose-Einstein-condensate superconductivity in iron chalcogenides. *Commun. Phys.* **6**, 183 (2023).
60. Agterberg, D. F., Brydon, P. M. R. & Timm, C. Bogoliubov Fermi surfaces in superconductors with broken time-reversal symmetry. *Phys. Rev. Lett.* **118**, 127001 (2017).
61. Setty, C., Bhattacharyya, S., Cao, Y., Kreisel, A. & Hirschfeld, P. Topological ultranodal pair states in iron-based superconductors. *Nat. Commun.* **11**, 523 (2020).
62. Shibauchi, T., Hanaguri, T. & Matsuda, Y. Exotic superconducting states in FeSe-based materials. *J. Phys. Soc. Jpn* **89**, 102002 (2020).
63. Vafek, O. & Chubukov, A. V. Hund interaction, spin-orbit coupling, and the mechanism of superconductivity in strongly hole-doped iron pnictides. *Phys. Rev. Lett.* **118**, 087003 (2017).
64. Okazaki, K. et al. Octet-line node structure of superconducting order parameter in KFe_2As_2. *Science* **337**, 1314–1317 (2012).
65. Wu, D. et al. Nodal $s_{\pm}$ pairing symmetry in an iron-based superconductor with only hole pockets. *Nat. Phys.* **20**, 571–578 (2024).

[1]Department of Physics, Yale University, New Haven, CT, USA. [2]Energy Sciences Institute, Yale University, West Haven, CT, USA. [3]Instituto de Física, Universidade Federal de Goiás, Goiânia, Brazil. [4]Department of Physics and Astronomy, University of California, Davis, CA, USA. [5]Gleb Wataghin Institute of Physics, University of Campinas, Campinas, Brazil. [6]Department of Physics, Fairfield University, Fairfield, CT, USA. [7]School of Physics and Astronomy, University of Minnesota, Minneapolis, MN, USA. [8]Department of Applied Physics, Yale University, New Haven, CT, USA. [9]Present address: Department of Physics, University of Illinois Urbana-Champaign, Urbana, Illinois, USA. [10]These authors contributed equally: Pranab Kumar Nag, Kirsty Scott.
✉e-mail: eduardo.dasilvaneto@yale.edu

Methods

Material synthesis and characterization

Single crystals of $FeSe_{0.81}S_{0.19}$ were grown using the chemical vapour transport method in a tilted furnace following the methods outlined in ref. 66. The actual sulfur concentration was determined by counting S atoms in STM topographic images. The S concentration of the samples was also characterized using a scanning electron microscope equipped with an energy-dispersive X-ray spectrometer. Several platelets with dimensions of 1–2 mm by 1–2 mm were selected for characterization.

STM and STS measurements

STM and STS measurements were obtained with a customized Unisoku USM-1300 instrument. The samples were cleaved in situ in an ultrahigh-vacuum environment with pressures below 10^{-9} torr. For all STS measurements (except those shown in Fig. 1e) the temperature sensor located at the STM head read 298 mK. At that thermometer temperature, the electronic temperature was estimated to be 520 mK based on Dynes fits to measurements of the superconducting gap on Pb. In Supplementary Fig. 1 we show tunnelling data acquired on Pb (temperature sensor reading 320 mK) and a Dynes fit function yielding an electronic temperature of 533 mK. In Fig. 1e, the temperatures indicated are the electronic temperatures estimated from the temperature dependence of the measurements on superconducting Pb.

STS parameters

Differential conductance measurements (dI/dV) used for Figs. 2–4 were acquired with a set point current and bias of 1.2 nA and −6 mV, respectively, over a 256 × 256 grid covering an area of 156 × 156 nm^2. The lock-in bias modulation for all those measurements was set to 50 μV. Topographic measurements acquired simultaneously with the spectroscopic maps are shown in Supplementary Fig. 2a,b. An additional topographic measurement with a higher spatial resolution (1,024 × 1,024) from nominally the same area is shown in Supplementary Fig. 2c.

STS data preprocessing

Before performing the discrete Fourier transformation of the real-space differential conductance maps, we subtracted the spatial average of the map for each energy. After carrying out the Fourier transformation, we used the four-fold symmetry of the sample to further suppress the influence of random tip geometries and to improve the signal-to-noise ratio overall. To better resolve the most salient features of the data and to improve the signal-to-noise ratio, the Fourier space images were also locally averaged using a Gaussian function (half-width at half-maximum of 2.5 pixels). Supplementary Figs. 3 and 4 demonstrate these steps.

Spectral analysis of the rounded-square feature

The results presented in Fig. 2k–l were derived from the data after the steps outlined above. As explained in the main text, we determined the angle-dependent DOS within the rounded-square pattern for different θ. For each θ and E, a spectral intensity value was obtained by averaging around the rounded-square contour for ±0.04 $Å^{-1}$ in the radial direction and ±0.008 $Å^{-1}$ in the perpendicular direction. The results are shown in Supplementary Fig. 5a,b. To highlight the superconducting gap we could either subtract (Supplementary Fig. 5c,d) or divide by (Supplementary Fig. 5e,f and Fig. 2k–l) a linear background from each curve. For each energy, the slope was determined from the data at ±1.15 meV.

Dispersion maps

For the data shown in Fig. 2a–j and for the dispersion maps shown in Fig. 3b–e, each real-space conductance map was also normalized by the standard deviation obtained over the entire map. This step facilitated tracking of the locations of various peaks in the dispersion maps by decreasing relative intensity variations between energies.

Data availability

All data that support the findings of this study are available from the corresponding author upon reasonable request. Source data are provided with this paper.

References

66. Böhmer, A. E., Taufour, V., Straszheim, W. E., Wolf, T. & Canfield, P. C. Variation of transition temperatures and residual resistivity ratio in vapor-grown FeSe. *Phys. Rev. B* **94**, 024526 (2016).

Acknowledgements

We thank A. Chubukov, L. Glazman and P. Sukhachov for fruitful discussions during the preparation of this manuscript. E.H.d.S.N. acknowledges support from the National Science Foundation under grant number DMR-2034345. This work was supported by the Alfred P. Sloan Fellowship (E.H.d.S.N.). Sample synthesis was supported by the UC Lab Fees Research Program (grant number LFR-20-653926). R.M.F. was supported by the US Department of Energy, Office of Science, Basic Energy Sciences, Materials Science and Engineering Division, under award number DE-SC0020045 (theory work). E.M. acknowledges support from CNPq-Brazil under grant number 309584/2021-3 and Fapesp under grant number 2022/15453-0.

Author contributions

P.K.N., K.S., M.W. and E.H.d.S.N. performed the STM measurements with the assistance of X.Y., A.G.G. and A.G. V.S.d.C., R.M.F. and E.M. performed theoretical calculations. X.Y. computed QPI simulations with assistance from A.G. and E.H.d.S.N. J.K.B. grew and characterized the $FeSe_{1-x}S_x$ crystals with support from P.K. and V.T. E.H.d.S.N., R.M.F., P.K.N., K.S., V.S.d.C., A.G. and E.M. wrote the manuscript with input from all other authors. E.H.d.S.N. conceived of the experiments and was responsible for overall project direction, planning and management.

Competing interests

The authors declare no competing interests.

Additional information

Extended data is available for this paper at https://doi.org/10.1038/s41567-024-02683-x.

Supplementary information The online version contains supplementary material available at https://doi.org/10.1038/s41567-024-02683-x.

Correspondence and requests for materials should be addressed to Eduardo H. da Silva Neto.

Peer review information *Nature Physics* thanks Lingyuan Kong for their contribution to the peer review of this work.

https://doi.org/10.1038/s41567-024-02683-x

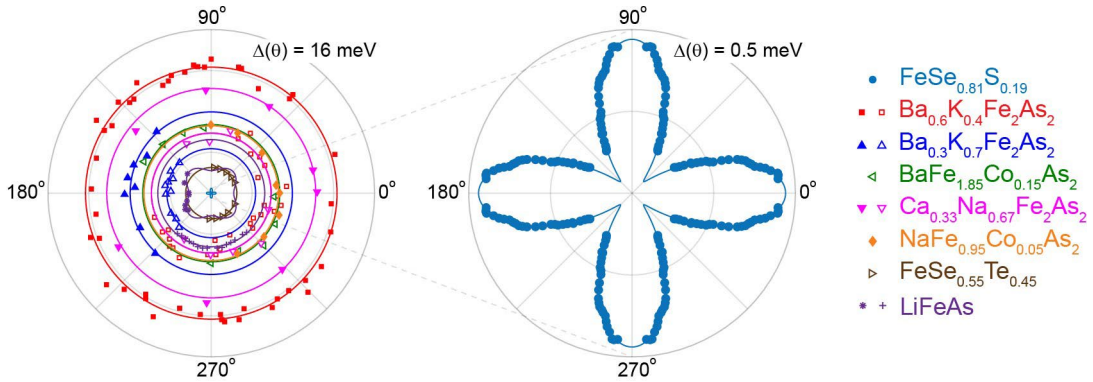

Extended Data Fig. 1 | Comparison to other tetragonal Fe-based Superconductors. Polar plots comparing $|\Delta(\theta)|$, the superconducting gap, in $FeSe_{0.81}S_{0.19}$ (outer hole pocket, full circles) and in various tetragonal FeSCs (reproduced from[35,36]). The gaps for the largest (stars[35]) and middle (crosses[36]) pockets at Γ in LiFeAs, which has three pockets, are depicted. For the other materials, open (full) symbols represent $|\Delta(\theta)|$ for outer (inner) hole pockets. For $FeSe_{0.81}S_{0.19}$ the line represents the fit to the form in Eq. (1) of the paper (see Fig. 4). For the largest hole pocket of LiFeAs, the line follows $\Delta = \Delta_0 + \Delta_1 \cos(4(\theta + \Phi))$, with $\Delta_0 = 2.6$ meV, $\Delta_1 = 0.4$ meV and $\Phi = \pi/4$ as reported[35]. For all other materials the lines are constant Δ curves, with their radii determined from the average experimental $\Delta(\theta)$.